Multiaxial Magneto-Mechanical Modelling of Electrical Machines with Hysteresis

P Rasilo*[†], U Aydin[†], D Singh[†], F Martin[†], R Kouhia[#], A Belahcen[†], A Arkkio[†]

**Tampere University of Technology (TUT), Department of Electrical Engineering, P.O. Box 692, FI-33101 Tampere, Finland*
[†]Aalto University, Department of Electrical Engineering and Automation, P.O. Box 13000 FI-00076 Aalto, Finland
[#]TUT, Department of Mechanical Engineering and Industrial Systems, P.O. Box 589, FI-33101 Tampere, Finland
E-mail: paavo.rasilo@tut.fi

Keywords: Eddy currents, finite element analysis, high speed machines, hysteresis, induction machines, magnetic materials, magnetoelasticity, permanent-magnet synchronous machines.

Abstract

We present a numerical method for modelling of coupled magneto-mechanical behaviour and magnetic hysteresis losses in electrical machine cores under mechanical stress. An energy-based single-valued magneto-mechanical constitutive law is coupled to the Jiles-Atherton model of hysteresis. The material model is implemented in a 2-D finite element method, which solves for both the magnetic vector potential and mechanical displacement in the electrical machine core. The model is applied to analyse stator shrink fitting in a permanent-magnet synchronous machine and centrifugal stress in a high-speed solid-rotor induction machine. The losses in the machines are shown to increase due to the consideration of the mechanical stress.

1 Introduction

The magnetic properties of ferromagnetic materials can be significantly altered by mechanical loading, which causes problems in design and analysis of electrical machines. Electrical machine cores are subject to stresses and deformations especially due to the manufacturing processes, e.g. punching, welding and shrink-fitting of the core laminations. In addition, thermal expansion, centrifugal forces and magnetic fields give rise to additional stresses during the operation of the machines. These stresses and deformations affect both the magnetization and power-loss properties of the core laminations, which is not taken into account in most of the analysis methods used today. This lack of coupled magneto-mechanical modelling tools is majorly associated with the fact that calculations often overestimate the efficiencies of the machines.

During the very recent years, an increasing amount of research has been devoted to overcome the aforementioned limitations [1]-[8]. In all the papers, finite element (FE) analysis tools were used to evaluate the magnetic field and the mechanical stress distributions in electrical machine cores. However, due to the complexity of the magneto-mechanical problem, the coupling between the magnetic and mechanical fields has been mostly experimental in nature. In [1], [2], [4] and [5], the magnetization properties and losses for a given stress were interpolated from large sets of measurements for parallel magnetic field and stress, while [5] and [8] replaced the interpolation by simplified scalar expressions.

The experimental approaches face problems especially when dealing with multiaxial fields. Depending on the location in the core, many different combinations of flux-density vectors and stress tensors, their magnitudes and relative orientations are present. To apply the uniaxial measurement results, [2] and [4] replaced the multiaxial stress by the Von Mises stress, while [5], [6] and [8] applied the magneto-elastic equivalent stress presented in [9]. However, the accuracy of these models suffers from using a scalar reluctivity in the presence of stress-induced anisotropy and from the application of scalar type iron-loss models with vector fields.

On the other hand, truly multiaxial magneto-mechanical material models are only starting to emerge. In [3], a simplified multiscale model was applied in FE analysis of a switched reluctance motor. In [7], also hysteresis losses were considered. In our earlier works, we have also developed a multiaxial energy-based single-valued (SV) constitutive law to describe the coupled magneto-mechanical behaviour of electrical steel sheets [10]. The model has also recently been coupled to the Jiles-Atherton (JA) model of hysteresis for modelling the effect of stress on the magnetic hysteresis losses [11]. The models of [7] and [11] account for the stress-induced phase shift between the magnetic field and magnetization vectors, and also allow modelling the hysteretic behaviour for vector magnetic fields with arbitrary time variation.

In this paper we implement the magneto-mechanical material model of [11] in a 2-D FE method for coupled magneto-mechanical analysis of electrical machines. The model is applied to evaluate the stator hysteresis losses in a 2.2-kW permanent-magnet synchronous motor (PMSM) and the effects of centrifugal stresses in the rotor of a 50-kW high-speed solid-rotor induction motor (SRIM). The core losses of the machines are shown to increase due to the consideration of the mechanical stresses. In the PMSM stator, the main loss mechanism is the direct effect of the stress on the hysteresis losses, while in the SRIM, the stress-induced permeability variation dominates.

2 Methods

2.1 Magneto-mechanical material model

The material model has recently been presented in [11], and is briefly summarised here. A Helmholtz free energy density ψ is expressed as a function of five scalar invariants depending on the flux-density vector $\boldsymbol{B}$ and the total strain tensor $\boldsymbol{\varepsilon}$:

$$I_1 = \mathrm{tr}\,\boldsymbol{\varepsilon}, \quad I_2 = \frac{1}{2}\mathrm{tr}\,\boldsymbol{\varepsilon}^2, \\ I_4 = \frac{\boldsymbol{B}\cdot\boldsymbol{B}}{B_{\mathrm{ref}}^2}, \quad I_5 = \frac{\boldsymbol{B}\cdot(\boldsymbol{\varepsilon}_{\mathrm{d}}\boldsymbol{B})}{B_{\mathrm{ref}}^2}, \quad I_6 = \frac{\boldsymbol{B}\cdot(\boldsymbol{\varepsilon}_{\mathrm{d}}^2\boldsymbol{B})}{B_{\mathrm{ref}}^2}, \tag{1}$$

where B_{ref} = 1 T. The invariants allow simplifying the multiaxial problem into a scalar problem of five variables. I_1 and I_2 describe purely elastic behaviour, and I_4 purely magnetic behaviour. I_5 and I_6 describe the magnetoelastic coupling, and are written using the deviatoric strain

$$\boldsymbol{\varepsilon}_{\mathrm{d}} = \boldsymbol{\varepsilon} - \frac{1}{3}(\mathrm{tr}\,\boldsymbol{\varepsilon})\boldsymbol{I}, \tag{2}$$

in which $\boldsymbol{I}$ is the unit tensor. The expression for $\psi(I_1, I_2, I_4, I_5, I_6)$ is given in the Appendix. The magnetic field strength and the magneto-elastic stress are obtained as

$$\boldsymbol{H}(\boldsymbol{B},\boldsymbol{\varepsilon}) = \left(\frac{\partial\psi(\boldsymbol{B},\boldsymbol{\varepsilon})}{\partial\boldsymbol{B}}\right)^{\mathrm{T}} \tag{3}$$

$$\boldsymbol{\sigma}(\boldsymbol{B},\boldsymbol{\varepsilon}) = \frac{\partial\psi(\boldsymbol{B},\boldsymbol{\varepsilon})}{\partial\boldsymbol{\varepsilon}} + \boldsymbol{\sigma}_{\mathrm{mag}}(\boldsymbol{B},\boldsymbol{H}(\boldsymbol{B},\boldsymbol{\varepsilon})), \tag{4}$$

where $\boldsymbol{\sigma}_{\mathrm{mag}}$ is the Maxwell stress tensor [11].

The SV model is coupled to the JA model of hysteresis [12]. The model is summarised as

$$\boldsymbol{H}_{\mathrm{eff}} = \boldsymbol{H} + a\boldsymbol{M}, \tag{5}$$

$$\boldsymbol{M}_{\mathrm{an}} = \boldsymbol{F}(\boldsymbol{H}_{\mathrm{eff}}), \tag{6}$$

$$\boldsymbol{d} = \boldsymbol{M}_{\mathrm{an}} - \boldsymbol{M}_{\mathrm{irr}} \text{ and } d = \frac{d\boldsymbol{B}}{dt}\cdot\boldsymbol{d}, \tag{7}$$

$$\frac{d\boldsymbol{M}_{\mathrm{irr}}}{d\boldsymbol{H}_{\mathrm{eff}}} = \begin{cases} \boldsymbol{k}(\boldsymbol{\varepsilon}_{\mathrm{d}})^{-1}\dfrac{\boldsymbol{d}\boldsymbol{d}^{\mathrm{T}}}{|\boldsymbol{d}|}, & \text{if } |\boldsymbol{d}| > 0 \text{ and } d > 0 \\ \boldsymbol{0}, & \text{otherwise,} \end{cases} \tag{8}$$

$$\frac{d\boldsymbol{M}}{d\boldsymbol{H}_{\mathrm{eff}}} = c\frac{d\boldsymbol{M}_{\mathrm{an}}}{d\boldsymbol{H}_{\mathrm{eff}}} + (1-c)\frac{d\boldsymbol{M}_{\mathrm{irr}}}{d\boldsymbol{H}_{\mathrm{eff}}}, \tag{9}$$

in which α and c are constant fitting parameters. Equation (6) is used to denote that the relationship between $\boldsymbol{M}_{\mathrm{an}}$ and $\boldsymbol{H}_{\mathrm{eff}}$ is the same as the relationship between $\boldsymbol{M}$ and $\boldsymbol{H}$ described by the Helmholtz energy. The coercive field is determined by the tensor parameter $\boldsymbol{k}$, which is made dependent on the deviatoric strain. An isotropic dependency leads to the expression

$$\boldsymbol{k}(\boldsymbol{\varepsilon}_{\mathrm{d}}) = k_0\left(\boldsymbol{I} + a\boldsymbol{\varepsilon}_{\mathrm{d}} + b\boldsymbol{\varepsilon}_{\mathrm{d}}^2\right), \tag{10}$$

in which k_0, a and b can depend at most on the scalar invariants of $\boldsymbol{\varepsilon}_{\mathrm{d}}$. In this paper, they are treated as constants.

The model parameters have been obtained by fitting to measured uniaxial SV and hysteretic magnetization curves. The parameters are given in the Appendix. Figure 1 (a) shows that the model is able to correctly predict the magnetization curves and hysteresis losses under uniaxial stresses and a parallel magnetic field. In order to illustrate the multiaxial behaviour, Figure 1 (b) shows the variation of the relative permeability under uniaxial, equibiaxial, hydrostatic and pure shear stresses. The magnitude of the stresses varies from 300 MPa compression (-) to 300 MPa tension (+). The results at compression and at small tensile stress are consistent with other recently presented multiaxial modelling results [13] and measurements [14]. In addition, it is seen that high tensile stress reduces the permeability from the zero-stress value, and that the hydrostatic stress has little effect on the permeability, which is consistent with magneto-elastic theories.

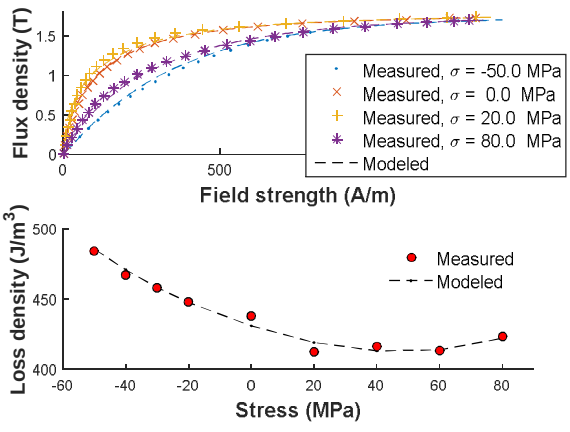

(a)

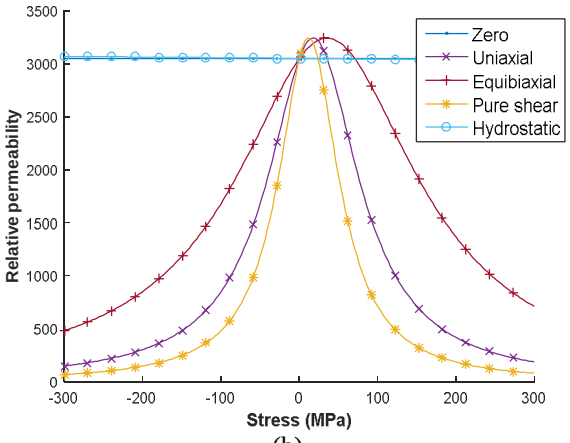

(b)

Figure 1: (a) Comparison of measured and modelled magnetization curves and hysteresis losses under uniaxial stresses and a parallel magnetic field. (b) Modelling results on the effect of different multiaxial stresses on the relative permeability at a constant flux-density of 1.5 T

2.2 Finite-element implementation

A 2-D cross section of a radial-flux electrical machine is considered in the x-y plane. The partial differential equations to be solved for in the iron core are

$$\nabla \times \boldsymbol{B} = 0 \tag{11}$$

$$\nabla \cdot \boldsymbol{H}(\boldsymbol{B}, \boldsymbol{\varepsilon}) = \boldsymbol{J} \tag{12}$$

$$\nabla \times \boldsymbol{\sigma}(\boldsymbol{B}, \boldsymbol{\varepsilon}) = \nabla \times \boldsymbol{\sigma}_0 - \boldsymbol{f}\,, \tag{13}$$

where $\boldsymbol{J}$ is the current density and $\boldsymbol{\sigma}_0$ and $\boldsymbol{f}$ are the initial stress and body force distributions, respectively. The Cartesian unit vectors are denoted $\boldsymbol{x}$, $\boldsymbol{y}$ and $\boldsymbol{z}$. To satisfy (11) strongly, a magnetic vector potential $\boldsymbol{A} = A\boldsymbol{z}$ is used. A plane strain configuration is assumed. The strain is expressed as a partial derivative of the in-plane displacement $\boldsymbol{U} = U_x\boldsymbol{x} + U_y\boldsymbol{y}$ and handled with the Voigt notation:

$$\boldsymbol{B} = \begin{bmatrix} \partial A/\partial y & -\partial A/\partial x \end{bmatrix}^{\mathrm{T}} \tag{14}$$

$$\boldsymbol{\varepsilon} = \begin{bmatrix} \partial U_x/\partial x & \partial U_y/\partial y & \partial U_x/\partial y + \partial U_y/\partial x \end{bmatrix}^{\mathrm{T}}, \tag{15}$$

in which the last strain term is $2\varepsilon_{xy}$.

This paper deals with both laminated and solid steel cores. The eddy-current density is expressed as

$$\boldsymbol{J} = \begin{cases} -\dfrac{k_{\mathrm{L}} d^2}{12} \nabla \cdot \dfrac{\partial \boldsymbol{B}}{\partial t}, & \text{in laminated steel} \\ -k_{\mathrm{S}} \dfrac{\partial \boldsymbol{A}}{\partial t}, & \text{in solid steel,} \end{cases} \tag{16}$$

in which d = 0.5 mm is the lamination thickness, and κ_{L} and κ_{S} denote the electrical conductivities. For the laminated steel, (16) yields the classical low-frequency approximation for the eddy currents. The conductivities used for the laminated and solid steel are 3 MS/m and 4.4 MS/m, respectively.

The vector potential and the displacement are expressed with nodal shape functions $\boldsymbol{N} = [N_1, N_2, \ldots]$ and nodal value vectors $\boldsymbol{a}$, $\boldsymbol{u}_x$ and $\boldsymbol{u}_y$, respectively The discrete derivative operations are written as

$$\boldsymbol{D}_{\mathrm{mag}}^{\mathrm{T}} = \begin{bmatrix} \partial \boldsymbol{N}/\partial y & -\partial \boldsymbol{N}/\partial x \end{bmatrix} \text{ and } \boldsymbol{D}_{\mathrm{mech}}^{\mathrm{T}} = \begin{bmatrix} \partial \boldsymbol{N}/\partial x & \boldsymbol{0} & \partial \boldsymbol{N}/\partial y \\ \boldsymbol{0} & \partial \boldsymbol{N}/\partial y & \partial \boldsymbol{N}/\partial x \end{bmatrix}, \tag{17}$$

so that

$$\boldsymbol{B} = \boldsymbol{D}_{\mathrm{mag}}\boldsymbol{a} \text{ and } \boldsymbol{\varepsilon} = \boldsymbol{D}_{\mathrm{mech}}\boldsymbol{u}\,, \text{ where } \boldsymbol{u} = \begin{bmatrix} \boldsymbol{u}_x \\ \boldsymbol{u}_y \end{bmatrix}. \tag{18}$$

Equations (12) and (13) are expressed weakly following the Galerkin method. For brevity, the integration over the solution domain is denoted with the angle brackets $\langle\cdot\rangle$ and the eddy-current terms for the laminated and solid regions are included in the same equation. The mass and damping of the core are accounted for in the mechanical equations by matrices $\boldsymbol{M}$ and $\boldsymbol{C}$, respectively. The resulting 2nd-order ordinary differential equation (ODE) system is reduced to a 1st-order ODE system by introducing additional equations to the nodal displacement velocities $\boldsymbol{v}$. The discrete coupled system to be solved thus becomes

$$\begin{aligned} &\left\langle \boldsymbol{D}_{\mathrm{mag}}^{\mathrm{T}} \left[\boldsymbol{H}(\boldsymbol{B}, \boldsymbol{\varepsilon}) + \frac{k_{\mathrm{L}} d^2}{12} \frac{\partial \boldsymbol{B}}{\partial t} \right] + k_{\mathrm{S}} \boldsymbol{N}^{\mathrm{T}} \frac{\partial \boldsymbol{A}}{\partial t} \right\rangle = \boldsymbol{0} \\ &\left\langle \boldsymbol{D}_{\mathrm{mech}}^{\mathrm{T}} \left[\boldsymbol{\sigma}(\boldsymbol{B}, \boldsymbol{\varepsilon}) - \boldsymbol{\sigma}_0 \right] \right\rangle + \boldsymbol{C}\boldsymbol{v} + \boldsymbol{M}\frac{d\boldsymbol{v}}{dt} = -\left\langle \begin{matrix} \boldsymbol{N}^{\mathrm{T}} \\ \boldsymbol{N}^{\mathrm{T}} \end{matrix} \boldsymbol{f} \right\rangle \\ &\frac{d\boldsymbol{u}}{dt} - \boldsymbol{v} = \boldsymbol{0}. \end{aligned} \tag{19}$$

The system is discretized in time with the implicit Euler method and solved iteratively with the Newton-Raphson (NR) method. The Jacobian matrix becomes

$$\begin{bmatrix} \left\langle \boldsymbol{D}_{\mathrm{mag}}^{\mathrm{T}} \left(\dfrac{\partial \boldsymbol{H}}{\partial \boldsymbol{B}} + \dfrac{k_{\mathrm{L}} d^2}{12\Delta t} \boldsymbol{I} + \dfrac{k_{\mathrm{s}}}{\Delta t} \boldsymbol{N}^{\mathrm{T}} \boldsymbol{N} \right) \right\rangle & \left\langle \boldsymbol{D}_{\mathrm{mag}}^{\mathrm{T}} \dfrac{\partial \boldsymbol{H}}{\partial \boldsymbol{\varepsilon}} \boldsymbol{D}_{\mathrm{mech}} \right\rangle & \boldsymbol{0} \\ \left\langle \boldsymbol{D}_{\mathrm{mech}}^{\mathrm{T}} \dfrac{\partial \boldsymbol{\sigma}}{\partial \boldsymbol{B}} \boldsymbol{D}_{\mathrm{mag}} \right\rangle & \left\langle \boldsymbol{D}_{\mathrm{mech}}^{\mathrm{T}} \dfrac{\partial \boldsymbol{\sigma}}{\partial \boldsymbol{\varepsilon}} \boldsymbol{D}_{\mathrm{mech}} \right\rangle & \boldsymbol{C} + \dfrac{1}{\Delta t}\boldsymbol{M} \\ \boldsymbol{0} & \dfrac{1}{\Delta t}\boldsymbol{I} & -\boldsymbol{I} \end{bmatrix}.$$

After forming the equations, the system is transformed into polar coordinates for easier handling of the boundary conditions. The field equations are coupled to the voltage equations of the stator and rotor windings in order to supply the machine from a voltage source. The rotor is rotated with constant speed and the air gap is remeshed at every time step. Linear FEs are used in all simulations. The hysteresis model could be straightforwardly applied during the field solution by calculating $\boldsymbol{H}$ and $\partial\boldsymbol{H}/\partial\boldsymbol{B}$ with the JA model. However, to our experience, inclusion of hysteresis in the solution causes convergence problems and doesn't significantly affect the accuracy. Thus only the SV model of Section 2.1 is used during the solution of the FE equations, and the JA model is applied at the post-processing stage to calculate the losses.

3 Application and results

3.1 Test machines

Two different electrical machines are simulated. The first machine is a 2.2-kW permanent-magnet synchronous motor (PMSM) and is used to evaluate the effect of shrink fitting on the stator losses. The second one is a 50-kW high-speed solid-rotor induction motor (SRIM) and is used to evaluate the effect of centrifugal stress on the eddy-current losses in the rotor. The rated datas and some dimensions of the machines are given in Table 1.

Data	PMSM	SRIM
Power	2.2 kW	50 kW
Voltage	370 V	400 V
Connection	delta	star
Speed	1500 rpm	100 000 rpm
Number of pole pairs	3	1
Stator outer diameter	165 mm	167 mm
Rotor outer diameter	102 mm	70 mm
Air gap	1 mm	3 mm

Table 1: Ratings and dimensions of the test machines.

Only the smallest required symmetry sector is solved, which means only one pole for each machine. The vector potential is fixed to zero on the outer boundary of the stator. The tangential displacement is fixed to zero at the outer boundary of the stator in the PMSM and at the outer boundary of the rotor steel in the SRIM. At the edges of the symmetry sector, antiperiodic and periodic boundary conditions are applied for the vector potential and the displacement, respectively.

3.2 Shrink fitting in permanent magnet machine

In shrink fitting, the outer boundary of the PMSM stator is displaced radially inwards due to the pressure caused by the frame. Displacements of 0–50 µm are considered. In the magneto-mechanical simulation, the radial displacement cannot be fixed since the machine has to be able to deform due to the magnetostriction. Thus, a purely mechanical simulation is first performed by fixing the vector potential to zero and the radial displacement of the stator boundary to the desired value. The obtained shrink-fitting stress distribution is then used as the source $\boldsymbol{\sigma}_0$ to the magneto-mechanical problem according to (13). Figure 2 shows the shrink-fitting stress distribution in the stator core at 50-µm radial compression.

Figure 3 (a) compares the simulated and measured terminal currents of the machine at different loads. The results without shrink fitting and at 50-µm compression are given. The shrink fitting increases the terminal currents especially at small loads when the magnetization properties have a more significant effect on the current. When shrink-fitting is considered, the simulated currents are closer to the measured ones. Figure 3 (b) shows the increase in the total electromagnetic losses of the machine due to 20- and 50-µm radial compressions. The losses comprise the stator copper losses, the hysteresis and eddy-current losses in the stator and rotor iron as well as the eddy-current losses in the magnets. At no-load the electromagnetic losses increase up to 19.8 %, but at the rated load the increase drops to 2.9 %.

The stator hysteresis loss is the most affected loss component due to the shrink fitting. The effect of the shrink-fitting stress on the hysteresis loss is twofold. First of all, the application of stress changes the permeability distribution in the core, which causes the flux-density distribution $\boldsymbol{B}(x,y)$ to differ from the zero-stress case. Due to the roughly quadratic

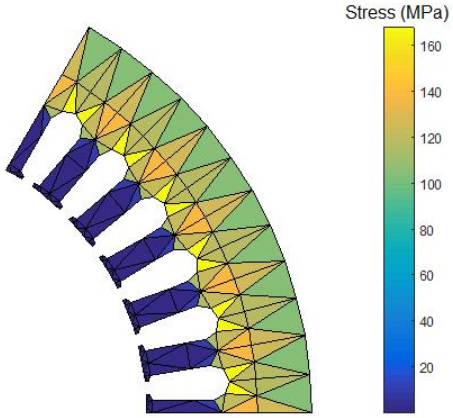

Figure 2: Shrink-fitting (Von Mises) stress distribution in the PMSM at 50-µm radial displacement.

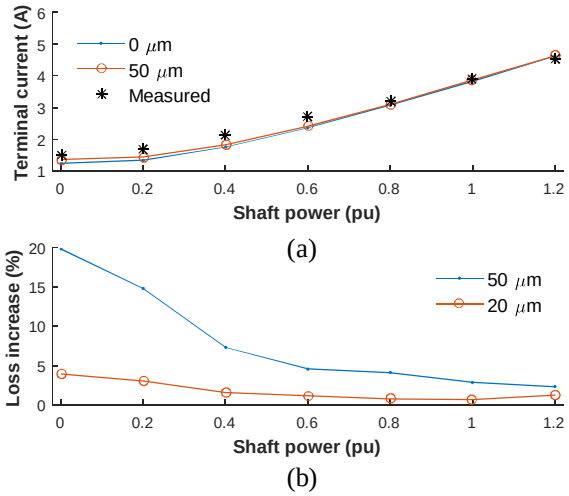

Figure 3: (a) Effect of the shrink-fitting on the terminal current of the PMSM and comparison to measurement results. (b) Increase in the total losses at two different shrink-fitting lengths compared to the unstressed case.

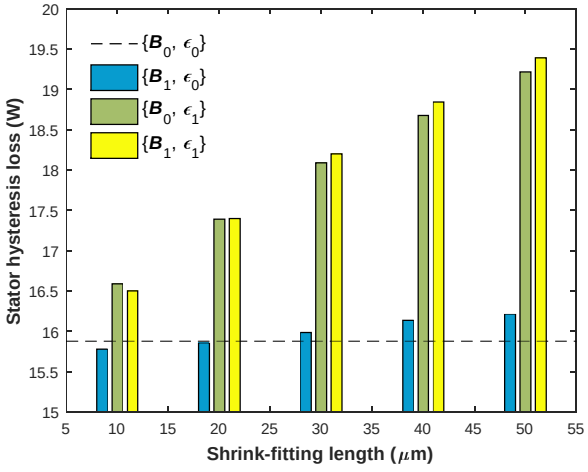

Figure 4: Effect of permeability variation and specific loss density increase on the stator hysteresis losses of the PMSM at different shrink-fitting lengths.

dependency of the hysteresis loss on $\mathsf{P}\boldsymbol{B}(x,y)\mathsf{P}$, more uneven flux-density distributions lead to increased core losses even if a stress-dependent hysteresis model was not considered. On the other hand, the deformation of the core also has a direct effect on the hysteresis losses as seen from Figure 1 (a). To analyse in what proportions these two phenomena affect the stator hysteresis losses, we perform the following study.

Let $\{\boldsymbol{B}_0, \boldsymbol{\varepsilon}_0\}$ denote the coupled field solution that has been obtained without shrink fitting and $\{\boldsymbol{B}_1, \boldsymbol{\varepsilon}_1\}$ the one that has been obtained with shrink fitting. By applying the hysteresis model in a post-processing manner, we are able to calculate the hysteresis losses with all the four solution combinations $\{\boldsymbol{B}_0, \boldsymbol{\varepsilon}_0\}$, $\{\boldsymbol{B}_1, \boldsymbol{\varepsilon}_0\}$, $\{\boldsymbol{B}_0, \boldsymbol{\varepsilon}_1\}$, and $\{\boldsymbol{B}_1, \boldsymbol{\varepsilon}_1\}$. Figure 4 shows the losses in each case. It is seen that the change in the flux density distribution (case $\{\boldsymbol{B}_1, \boldsymbol{\varepsilon}_0\}$) changes the loss only a little while the most dominant effect is the direct effect of the strain on the hysteresis loop (case $\{\boldsymbol{B}_0, \boldsymbol{\varepsilon}_1\}$). This justifies also the application of the hysteresis model only in the post-processing stage of the calculation.

3.3 Centrifugal stress in high-speed machine

The second machine is a high-speed SRIM designed for a milling cutter application. The rotor is made of high-strength construction steel, and the center part of the rotor has been left hollow to allow attaching the cutter blade. This, however, significantly increases the centrifugal stress compared to a solid cylinder. The rotor surface is coated with a 1-mm copper layer, in which most of the rotor losses occur.

The magnetization properties of the rotor steel have only been measured at zero stress. In order to identify the magneto-mechanical model, the stress-dependent B-H curves measured for the FeSi steel (Figure 1 (a)) were first scaled so that the zero-stress curve corresponds to the one measured for the rotor steel. The magnetomechanical model was then fitted to these scaled stress-dependent B-H curves.

The centrifugal force is added to (13) as a body force density $\boldsymbol{f}(r) = \rho r\omega^2 \boldsymbol{r}$, where ρ = 7800 kg/m^3 is the mass density of the steel, ω is the mechanical angular speed of the rotor, and r and $\boldsymbol{r}$ are the radial coordinate and the radial unit vector, respectively. Figure 5 shows the resulting centrifugal stress distribution at 100 000 rpm.

The SRIM was simulated both with and without the centrifugal stress. An initial state for the time-stepping simulations was calculated with a time-harmonic solution, in which the slip was selected so that the output power was the rated 50 kW. The supply voltage waveform contains one 120° voltage pulse per one half cycle. Figure 6 segregates the total electromagnetic losses and shows how the loss components change due to the inclusion of the centrifugal stress in the simulations. As expected, the mostly affected loss component is the eddy-current loss in the rotor iron. This means that contrary to Figure 4, the change of the permeability distribution due to the stress dominates in the SRIM. However, most of the rotor losses occur in the copper coating, whose losses are not much affected. The rotor hysteresis losses are negligible. The change in the stator copper losses is partly caused by the fact that since the slip is constant for both simulations, the powers are slightly different, 48.9 and 49.9 kW without and with centrifugal stress, respectively.

3.3 Computational performance

The FE model converges and performs reasonably well. The PMSM model consisted of 580 linear elements, from which 389 belonged to the laminated regions. The machine was simulated for 4 periods with 1000 time steps per period. On average, 5 NR iterations were required per time step, and the simulation time was about 0.255 s/step. The SRIM model consisted of 2656 linear elements, from which 1648 belonged to the solid rotor. The machine was simulated for 4 periods with 400 time steps per period. On average, 3 NR iterations were required per time step, and the simulation time was about 1.65 s/step.

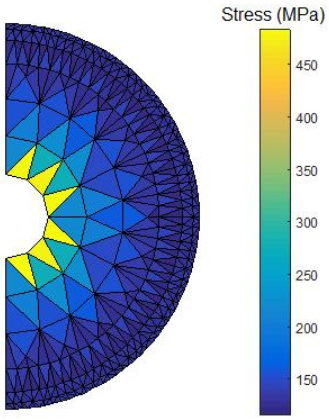

Figure 5: Centrifugal (Von Mises) stress distribution in the SRIM at 100 000 rpm.

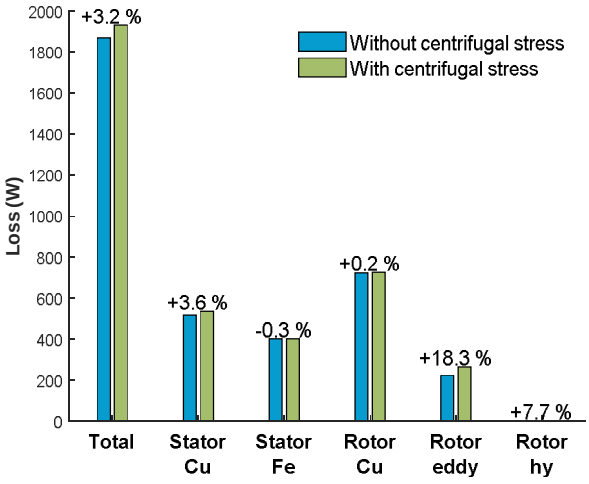

Figure 6: Segregation of the SRIM losses and their change due to the consideration of the centrifugal stress.

4 Discussion and conclusion

A finite-element implementation of a coupled multiaxial magneto-mechanical model was presented and applied to analyse the performance and losses in a permanent magnet machine and in a high-speed solid rotor induction machine.

The effects of the stress on the performance of the two machines could be seen as rather small, and a question might arise if coupled magneto-mechanical modelling is really needed. However, based on the literature, there seems to be large variations in the effects of the mechanical loading on the magnetization properties between different material grades. Thus it is difficult to generalize the results to other machines or materials. Nevertheless the developed model has been found as a suitable tool to account for the magneto-mechanical effects in electrical machines. The material model presented in Section 2.1 and [11] has been developed in a very general form, and thus its parameters should be rather easy to fit also for other materials.

Acknowledgements

The Academy of Finland is acknowledged for financial support. The research leading to these results has received funding from the European Research Council under the European Union's Seventh Framework Programme (FP7/2007-2013) / ERC grant agreement n°339380.

References

[1] K. Fujisaki, R. Hirayama, T. Kawachi, S. Satou, C. Kaidou, M. Yabumoto, T. Kubota, "Motor Core Iron Loss Analysis Evaluating Shrink Fitting and Stamping by Finite-Element Method," *IEEE Trans. Magn.*, Vol. 43, No. 5, pp. 1950-1954, May 2007.

[2] D. Miyagi, N. Maeda, Y. Ozeki, K. Miki, N. Takahashi, "Estimation of Iron Loss in Motor Core With Shrink Fitting Using FEM Analysis," *IEEE Trans. Magn.*, Vol. 45, No. 3, pp. 1704-1707, March 2009.

[3] L. Bernard, X. Mininger, L. Daniel, G. Krebs, F. Bouillault, M. Gabsi, "Effect of Stress on Switched Reluctance Motors: A Magneto-Elastic Finite-Element Approach Based on Multiscale Constitutive Laws," *IEEE Trans. Magn.*, Vol. 47, No. 9, pp. 2171-2178, September 2011.

[4] K. Yamazaki, Y. Kato, "Optimization of High-Speed Motors Considering Centrifugal Force and Core Loss Using Combination of Stress and Electromagnetic Field Analyses," *IEEE Trans. Magn.*, Vol. 49, No. 5, pp. 2181-2184, May 2013.

[5] K. Yamazaki and Y. Kato, "Iron loss analysis of interior permanent magnet synchronous motors by considering mechanical stress and deformation of stators and rotors," *IEEE Trans. Magn.*, Vol. 50, No. 2, Art. no 7022504, February 2014.

[6] K. Yamazaki, W. Fukushima, "Loss Analysis of Induction Motors by Considering Shrink Fitting of Stator Housings," *IEEE Trans. Magn.*, Vol 51, No. 3, Art. no. 8102004, March 2015.

[7] L. Bernard, L. Daniel, "Effect of Stress on Magnetic Hysteresis Losses in a Switched Reluctance Motor: Application to Stator and Rotor Shrink Fitting," *IEEE Trans. Magn.*, Vol. 51, No. 9, Art. no 7002513, September 2015.

[8] H. Ebrahimi, Y. Gao, H. Donozo, K. Muramatsu, T. Okitsu, D. Matsuhashi, "Effects of Stress and Magnetostriction on Loss and Vibration Characteristics of Motor," *IEEE Trans. Magn.* (in press).

[9] L. Daniel, O. Hubert, "An equivalent stress for the influence of multiaxial stress on the magnetic behavior," *J. Appl. Phys.*, Vol. 105, Art. no. 07A313, February 2009.

[10] K. Fonteyn, A. Belahcen, R. Kouhia, P. Rasilo, A. Arkkio, "FEM for Directly Coupled Magneto-Mechanical, Phenomena in Electrical Machines," *IEEE Trans. Magn.*, Vol. 46, No. 8, pp. 2923-2926, August 2010.

[11] P. Rasilo, D. Singh, U. Aydin, F. Martin, R. Kouhia, A. Belahcen, A. Arkkio, "Modeling of Hysteresis Losses in Ferromagnetic Laminations under Mechanical Stress," *IEEE Trans. Magn.* (in press).

[12] J. Gyselinck, P. Dular, N. Sadowski, J. Leite, J. P. A. Bastos, "Incorporation of a Jiles-Atherton vector hysteresis model in 2D FE magnetic field computations," *COMPEL*, Vol. 23, No. 3, pp. 685-693, 2004.

[13] L. Daniel, "An Analytical Model for the Effect of Multiaxial Stress on the Magnetic Susceptibility of Ferromagnetic Materials," *IEEE Trans. Magn.*, Vol. 49, No. 5, pp. 2037-2040, May 2013.

[14] L. Daniel, O. Hubert, M. Rekik, "A Simplified 3-D Constitutive Law for Magnetomechanical Behavior," *IEEE Trans. Magn.*, Vol. 51, No. 3, Art no. 7300704, March 2015.

Appendix

The Helmholtz energy is expressed using the five invariants as

$$y = \frac{\lambda I_1^2}{2} + 2\mu I_2 + \sum_{i=0}^{n_\alpha - 1} \frac{a_i}{i+1} \exp\left(\frac{\alpha_i (i+1)}{3} I_1\right) I_4^{i+1} + \kappa \sum_{i=0}^{n_\beta - 1} \frac{b_i}{i+1} I_5^{i+1} + \sum_{i=0}^{n_\gamma - 1} \frac{g_i}{i+1} I_6^{i+1}. \quad (20)$$

The expression is the same as was used in [11] except for the scaling of the parameters. Discussion on the form of (20) can be found in [10] and [11].

The parameters used in Fig. 1 are λ = 145 GPa, μ= 68.3 GPa, n_α = 9, n_β = 2, n_γ = 1, $\alpha_{0,\ldots,8}$ = 27.3, -79.5, 598, -1436, 1815, -1293, 523, -112, and 9.93 J/m^3, $\beta_{0,1}$ = -189 kJ/m^3 and 106 MJ/m^3, and γ_0 = 851 MJ/m^3, k_0 = 76.5 A/m, a = -0.274, and b = 0.432.